


# Reconfigurable and self-biased magnonic metamaterials

Cite as: J. Appl. Phys. **128**, 240902 (2020); <https://doi.org/10.1063/5.0033254>

Submitted: 15 October 2020 • Accepted: 05 December 2020 • Published Online: 23 December 2020

 Arabinda Haldar and  Adekunle Olusola Adeyeye

## COLLECTIONS

 This paper was selected as Featured



View Online



Export Citation



CrossMark

## ARTICLES YOU MAY BE INTERESTED IN

### Introduction to spin wave computing

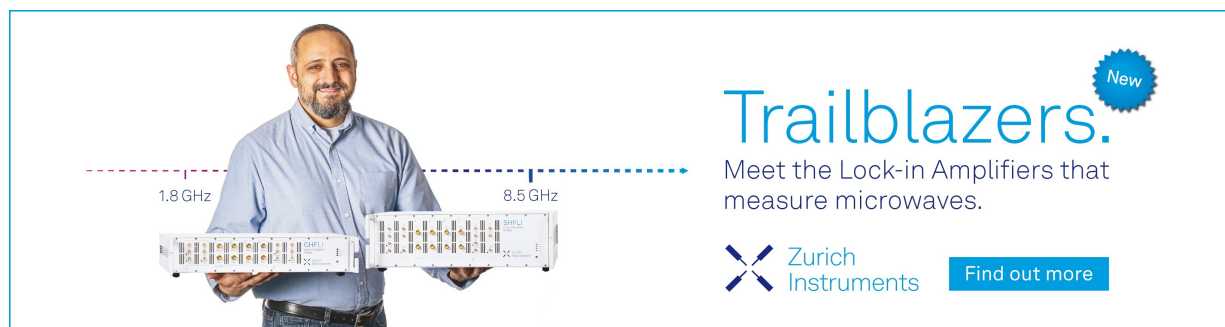
Journal of Applied Physics **128**, 161101 (2020); <https://doi.org/10.1063/5.0019328>


### Magnetization dynamics of nanoscale magnetic materials: A perspective

Journal of Applied Physics **128**, 170901 (2020); <https://doi.org/10.1063/5.0023993>


### The design and verification of MuMax3

AIP Advances **4**, 107133 (2014); <https://doi.org/10.1063/1.4899186>



**Trailblazers.** 

Meet the Lock-in Amplifiers that measure microwaves.

 Zurich Instruments [Find out more](#)

# Reconfigurable and self-biased magnonic metamaterials

Cite as: J. Appl. Phys. 128, 240902 (2020); doi: 10.1063/5.0033254

Submitted: 15 October 2020 · Accepted: 5 December 2020 ·

Published Online: 23 December 2020



View Online



Export Citation



CrossMark

Arabinda Haldar<sup>1,a)</sup>  and Adekunle Olusola Adeyeye<sup>2</sup> 

## AFFILIATIONS

<sup>1</sup>Department of Physics, Indian Institute of Technology Hyderabad, Kandi 502285, Telangana, India

<sup>2</sup>Department of Physics, Durham University, South Road, Durham DH1 3LE, United Kingdom

<sup>a)</sup>Author to whom correspondence should be addressed: [arabinda@phy.iith.ac.in](mailto:arabinda@phy.iith.ac.in)

## ABSTRACT

In magnonics, magnetic waves and oscillations are exploited for signal and information processing at microwave frequencies. A magnonic metamaterial is employed to configure different microwave bands by spatial engineering of magnetizations using different magnetic states or magnetic couplings. Magnetic field hysteretic variation of microwave responses has conventionally been used for tunable microwave operations. The use of such bias magnetic fields hinders the device integration of microwave magnonic devices. Here, we discuss a route to eliminating the requirement of bias magnetic field and simple initialization process for reconfigurable microwave operations. The distinct microwave responses are associated with different remanent magnetic states which are engineered by shape induced magnetic anisotropy rather than the conventional dipolar coupling driven magnetic states. However, the origin of the shift in the microwave spectra is associated with the variation of dipolar coupling for nanomagnetic networks, multilayer nanomagnets, and their arrays. This perspective provides an outlook on current challenges and potential future scopes of magnonic devices. We discuss some of our recent demonstrations toward the realizations of reconfigurable magnonic devices without any external bias magnetic field. Self-biased nanomagnets are also shown to have applications in designing a waveguide for spin wave transport and spin wave gating which operates without any bias magnetic field.

Published under license by AIP Publishing. <https://doi.org/10.1063/5.0033254>

## I. INTRODUCTION

Spintronic devices which make use of the spin degree of freedom of electrons have emerged as a promising alternative in post-CMOS (complementary metal oxide semiconductor) technologies.<sup>1–5</sup> Magnonics—a sub-area of spintronics—is focused on utilizing spin waves and oscillations for high frequency communication technologies. Here, a magnon—quanta for spin waves—carries the information in a magnetic medium such as magnetic films or patterned magnetic waveguides.<sup>6–13</sup> Such wave-based information processing offers extra functionalities like controlling both the amplitude and phase of the waves.<sup>14–16</sup> Additionally, the reconfiguration of magnetization and magnetic waves is less involved in comparison to their counterparts such as photonic materials. However, there are at least two major challenges in the current microwave magnonic devices, namely, microwave devices such as filters, circulators, phase shifters, delay lines, etc. are made from thick films or pellets and material operations require an external magnetic field for biasing.<sup>17</sup> A strong permanent magnet is used for such biasing purposes. The

size of the magnet increases with the increasing operating frequency. The stray field from such strong magnets can influence its immediate surroundings, thereby making it susceptible to magnetic fluctuations. Thus, both the size and bias magnetic field hinders the on-chip integration of microwave components.

Thin film fabrication and patterning of magnetic materials are essential in the realization of monolithic-integration of microwave devices and disruptive technologies totally based on wave-based information processing. Recently, the development of magnonic crystals (MCs)—magnetic counterpart of photonic crystals—has paved way for engineering spin wave bands by a periodic variation of magnetization.<sup>18–22</sup> Several magnonic crystals have been demonstrated based on the arrays of interacting nanodots,<sup>23–25</sup> antidots,<sup>26–30</sup> bi-components crystals,<sup>31–35</sup> lattice symmetry,<sup>36–39</sup> alternate width stripes,<sup>40,41</sup> and etched grooves.<sup>42</sup> Spin waves tailored by physical structuring in magnonic crystals are potentially good for the miniaturization of microwave electronics and signal processing devices. However, most of the tunable microwave operations

primarily utilize hysteretic quasi-uniform magnetization states by varying the external bias magnetic field, which limits the advantages of magnonics that it has promised to offer. On the other side, an intensive research to eliminate the bias field have led to the development of microwave components based on self-biased magnetic ferrites such as bismuth hexaferrite, which has strong perpendicular magnetic anisotropy along its  $c$  axis.<sup>43,44</sup> Such self-bias thick films enable the realization of 2D planar sub-cm size microwave components which can potentially be integrated, for example, in transmit/receive modules along with the active components.<sup>45</sup> However, such ferrite films are not yet suitable for patterning, thereby limiting further miniaturization beyond a sub-cm size.

The primary requirement for the miniaturization of microwave devices is the elimination of the need for bias magnets in patterned magnetic nanostructures. Recently, experimental demonstration of a circulator operation has been shown using axially magnetized nanopillars made from an alumina template, and the results are promising for the suitability of self-biased magnetic nanostructures for microwave devices.<sup>46</sup> An additional functionality which is of great importance is reconfigurable microwave properties along with bias field-free operations based on magnetic nanostructures. Examples of such systems are arrays of physically isolated but dipolar coupled nanopillars.<sup>47–50</sup> An antiferromagnetic (AFM) type magnetic ordering has been stabilized by applying a carefully designed initializing field along the short axis direction. On the other hand, a simple long axis initialization stabilized a ferromagnetic (FM) type remanent state. A large shift in the ferromagnetic resonance (FMR) spectra between FM and AFM remanent states has been recorded in such a magnetic system. Another example is based on dipolar coupled nanowires where AFM ordering are obtained, when the nanowires are initialized along their short axis. FM ordering at remanence is obtained by applying a magnetic field along the easy/long axis.<sup>51–53</sup> The dynamic spectra associated with the AFM remanent state does only not shift the FMR spectra but also open up gaps in the spin wave dispersion. Different remanent states stabilized through minor hysteresis loops are also found to be interesting in realizing distinct FMR responses. The results show the possibility of using such reconfigurable FMR responses in the logic operation.<sup>54,55</sup> However, dipolar coupling and minor loop hysteresis driven magnetic remanent states are sensitive to fabrication defects and require complex initialization processes. Recently, there are developments of other external controls for variations of magnetizations such as laser heating,<sup>56,57</sup> use of the hot tip of a scanning probe microscope,<sup>58</sup> and current induced Oersted field.<sup>59</sup>

In this perspective, we discuss an alternative solution to these outstanding challenges in reconfigurable magnonics and present some of our recent demonstrations. We first highlight the strategy for obtaining multiple remanent states based on shape induced magnetic anisotropies instead of dipolar coupling driven architectures. In order to obtain the desired remanent states, we use a simple field initialization scheme which can be implemented by using a sub-ns pulse field. This is in sharp contrast with the previous demonstrations where complex initialization schemes or a minor loop hysteresis have been used. We should also emphasize the fact that the remanent states obtained through shape induced anisotropy are more reproducible over a large area without defects.

This is a major challenge in dipolar coupling driven remanent states. One of our first key results based on a network of two rhomboid nanomagnets (RNMs) have been explained.<sup>60</sup> We demonstrate an unprecedented control of designing strategies in our demonstrations. We show that one can design different types of complex two-dimensional (2D) anti-parallel states<sup>61</sup> including a ferrimagnetic-type<sup>62</sup> state using the RNMs beyond their networks. We discuss how one can enhance the frequency shift in the FMR spectra by designing multi-layers of the RNMs and operation based on a single multilayer nanomagnet is experimentally demonstrated.<sup>63–65</sup> In all the above mentioned examples, dynamic responses and their tunable operation have been carried out at remanent states without the need for a bias magnetic field—a bottleneck for device integration—has been resolved. Furthermore, we have discussed the use of such self-biased RNMs in a magnonic device for spin wave transport and gating.<sup>66,67</sup> The results may pave way for the successful realization of nano-magnonic devices and on-chip microwave technologies. Finally, we emphasize the open questions and our perspective on the future roadmap for reconfigurable magnonic devices.

## II. RHOMBOID NANOMAGNETS

Self-biased nanomagnets with controlled multiple remanent states are the building blocks of a bias-free miniaturized microwave device. In addition, here we aim to achieve multiple remanent states driven by shape induced anisotropy rather than dipolar coupling driven architectures. Such nanomagnets are elusive. After an intensive search for appropriate nanostructures, we have shown in Ref. 60 that dipolar coupled rhomboid shaped nanomagnetic networks are suitable for this application. In order to understand the results better, we briefly introduce a single RNM and its magnetization reversal processes. A schematic of the RNM is shown in Fig. 1(a). The dimensions of the RNMs are  $300 \times 130 \times 25 \text{ nm}^3$  ( $u \times w \times t$ ), where  $u$ ,  $w$  are the sides of the RNMs and  $t$  is the thickness. The angle of the slanted edge ( $\theta$ ) is  $32^\circ$ . Two different orientations of the RNMs (P-type and Q-type) are shown in Fig. 1(b) along with a rectangular nanomagnet (R-type) for comparison. Simulated remanent states are obtained by applying an initialization field ( $H_i$ ) along the geometrical short axis ( $x$  axis) followed by the removal of the field, i.e.,  $H_i: 2000 \text{ Oe} \rightarrow 0$ . One can find that the P-type magnet points upward ( $\uparrow$ ) and Q-type magnet has downward ( $\downarrow$ ) magnetization. On the other hand, R-magnet has a multi-domain with arbitrary net magnetization ( $\uparrow$  or  $\downarrow$ ). Thus, a RNM has a unique magnetic remanent state for the different field initialization processes as compared to a rectangular nanomagnet. Experimental remanent magnetic configurations of the RNMs are shown as the magnetic force microscopy (MFM) images in Fig. 1(c), and the results are consistent with the simulated states [Fig. 1(b)]. On the other hand, rectangular magnets are found to have vortex configurations at random locations [Fig. 1(d)]. Such errors or unpredictable magnetic states are absent in the RNMs in a large area pattern. This deterministic magnetic orientation in RNMs is due to the fact that the energy maxima (hard) and minima (easy) of the RNMs do not lie along the geometrical short and long axes, respectively [Fig. 1(e)]. A deviation ( $\Delta\varphi$ ) of about  $10^\circ$  between the magnetic hard and geometrical short axis can be found. The short and long axes hysteresis loops

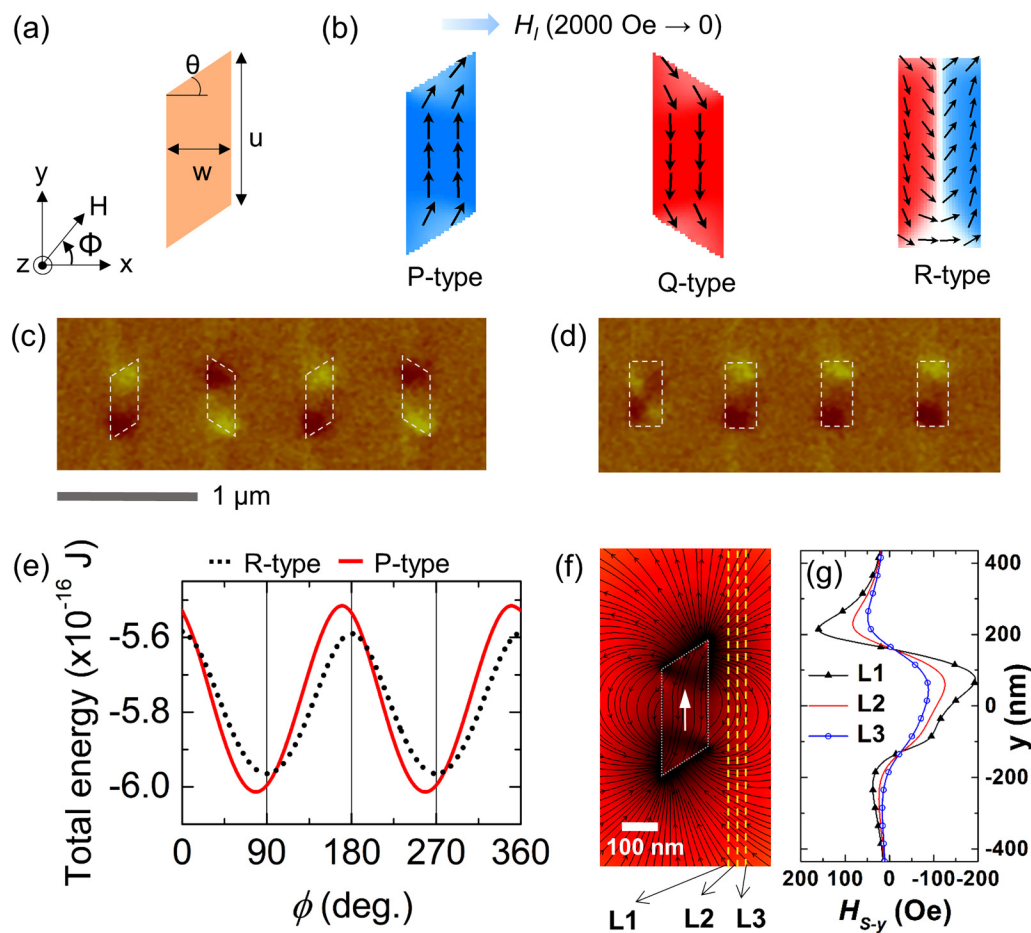


**FIG. 1.** (a) Schematic of a RNM structure. (b) Simulated remanent states of the P-type and Q-type RNMs for  $x$  axis initialization. Remanent state of a rectangular (R-type) nanomagnet is shown for the same initialization process. MFM images at remanence for (c) RNMs and (d) rectangular NMs. (e) Total energy as a function of angle  $\varphi$  showing the difference between magnetic hard axis and geometric short axis. (f) Stray field from an isolated RNM. (g) Line scans of the stray field along L1, L2, and L3. Reproduced with permission from Halder and Adeyeye, ACS Nano 10, 1690–1698 (2016). Copyright 2016 ACS Publishing LLC.

reveal that the switching field for the RNMs lies below 1000 Oe, and the saturation field is close to 1000 Oe. Note that the lower limit of the initialization field is the saturating field ( $H_{sat}$ ) which can be further optimized by the choice of dimensions, materials, and type of  $H_i$  (pulse field). In the following sections, different networks of RNMs will be discussed, and, therefore, we first estimate the stray field from the two-dimensional (2D) profiles of the stray field [Fig. 1(f)] and line scans at different positions away [50 nm (L1), 75 nm (L2), and 100 nm (L3)] from the RNM [Fig. 1(g)]. The maximum value of the stray field varies from 200 Oe to 100 Oe at a distance from 50 nm to 100 nm.

### III. DIPOLAR COUPLED NETWORKS OF RNMs

In order to realize the tunable operation without a bias magnetic field, we need to have at least two different remanent states

with significant variation in the effective field. Dipolar field driven FMR spectral shift is one such route which have been proposed in the past.<sup>47–53</sup> We have also proposed the tunable microwave properties based on dipolar coupling by engineering different magnetic configurations using both P- and Q-type of RNMs. Note that the remanent states in our proposed devices are driven by the shape induced anisotropy, whereas dipolar coupling only governs remanent states in earlier reports.

A dipolar coupled network (PQ) is shown in Fig. 2(a) which consist of P- and Q-type RNMs. The inter-element separation ( $\delta$ ) is 50 nm. These specific combinations were used to create two different controlled remanent states as shown in the simulated remanent states. FM-type ( $\uparrow\uparrow$ ) and AFM-type ( $\uparrow\downarrow$ ) magnetic states can be found for the  $y$  axis and  $x$  axis initializations ( $H_i$ : 2000 Oe  $\rightarrow$  0), respectively. For simplicity of discussion in what to follow, the remanent states are denoted by Y-state and X-state for  $y$  axis and  $x$  axis initializations,

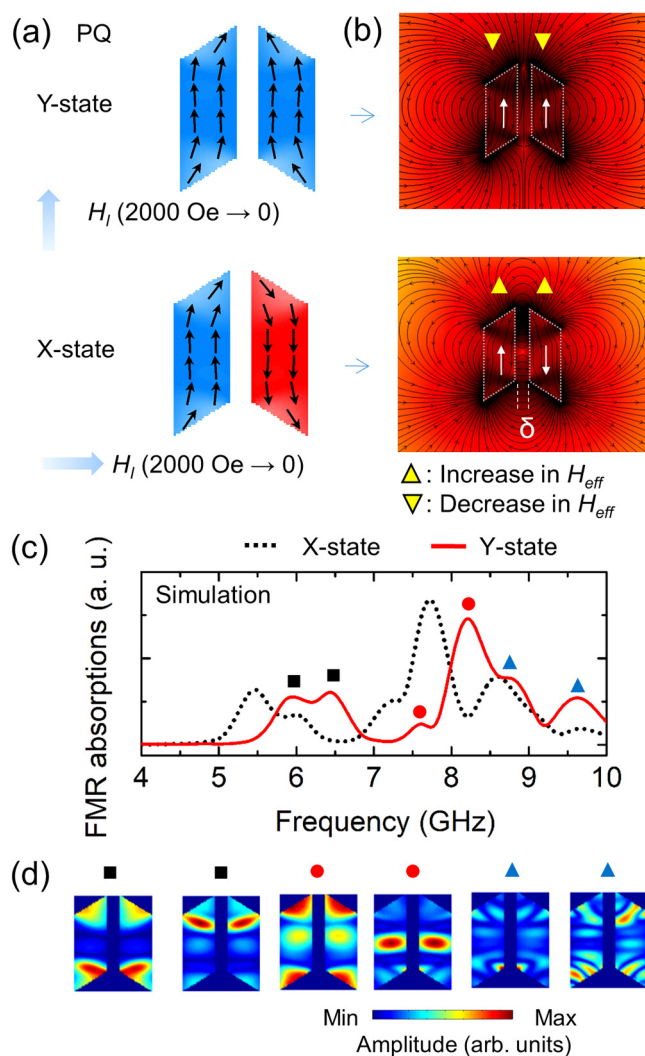


**FIG. 2.** (a) Simulated remanent states of a PQ network at Y-state (parallel) and X-state (anti-parallel) for  $y$  axis and  $x$  axis initializations, respectively. (b) Simulated demagnetization field distributions for PQ network at Y-state and X-state remanent states. The gap ( $\delta$ ) between the coupled P- and Q-magnets is 50 nm. (c) Simulated FMR spectra for the PQ network. (g) Simulated spatial profiles of the resonant modes as marked in the spectra with different symbols. Reproduced with permission from Halder and Adeyeye, ACS Nano **10**, 1690–1698 (2016). Copyright 2016 ACS Publishing LLC.

respectively. Note that we have also explored, in Ref. <sup>60</sup> other networks where X-states show up-down-up ( $\uparrow\downarrow\uparrow$ ) and up-up-down ( $\uparrow\uparrow\downarrow$ ) magnetizations for PQP and PPQ networks, respectively.<sup>60</sup> We emphasize here that the stray field from the RNMs does not affect the remanent states and thus, RNMs offer unprecedented control on the different types of anti-parallel states for the X-state.

Importantly, the stray field variation between the X-state and Y-state is of our interest for tunable microwave operations. Figure 2(b) shows the 2D distributions of the stray fields for both the remanent

states. One can notice that the  $y$ -component of the stray field ( $H_{S,y}$ ) which governs the effective magnetic field ( $H_{eff}$ ) inside the nanomagnets is aligned in the opposite way between the X-state and Y-state. The increase and decrease in  $H_{eff}$  are pictorially shown in Fig. 2(b). The X-state is found to have a higher effective field as the stray field aligns with the magnetization directions. It results in different dynamic responses for X-state and Y-state. Simulated FMR spectra for both remanent states are shown in Fig. 2(c). The modes are identified by plotting 2D spatial maps of the prominent modes in Fig. 2(d). We have denoted the modes which are concentrated near the edges ( $\blacksquare$ ) and the center ( $\bullet$ ) of the nanomagnets as edge mode and center mode, respectively. The mode at the highest frequency ( $\blacktriangle$ ) has nodal lines across the nanomagnets. Note that this mode only appears at low field regions ( $-600 \text{ Oe} < H_{app} < 600 \text{ Oe}$ ). However, the edge and center modes persist over the full field cycle ( $-1400 \text{ Oe} \rightarrow 0 \rightarrow 1400 \text{ Oe}$ ).<sup>60</sup>

The dynamic responses have been recorded from an isolated PQ network by using micro-focused Brillouin light scattering (micro-BLS) technique as shown in Fig. 3(a). In this approach, a 532-nm green laser is focused by using a 100 $\times$  objective lens down to approximately 300 nm spot diameter. The sample is placed on a nanostage for 2D scanning of the sample under the laser spot. Scattered laser beam is analyzed by a tandem Fabry-Pérot interferometer (TFPI). Shown in Fig. 3(b) are the PQ networks which are placed on top of a shorted ground-signal-ground (GSG) type co-planar waveguide (CPW) in order to excite the RNMs using radio frequency (RF) current (4–10 GHz). Micro-BLS spectra are shown in Fig. 3(c) for the X-state ( $\uparrow\downarrow$  or  $\downarrow\uparrow$ ) and the Y-state ( $\uparrow\uparrow$  or  $\downarrow\downarrow$ ). The most prominent mode is found at 7.3 GHz and 6.9 GHz for the X-state and the Y-state, respectively, resulting in a frequency shift ( $\Delta f$ ) of 400 MHz. The frequency shift is defined as  $\Delta f = f(\text{X-state}) - f(\text{Y-state})$ . One can design the XOR logic by defining a logical output as the response at 7.3 GHz and the inputs (0 or 1) being the magnetic states either  $\uparrow$  or  $\downarrow$ . It is noteworthy here that a single isolated RNM has the most prominent mode at 7 GHz.

In order to account for the above mentioned frequency shift, we have utilized Kittel's equation<sup>68</sup>

$$f_{res} = \frac{\gamma}{2\pi} \sqrt{(H_{eff} + (N_x - N_y)M_y)(H_{eff} + (N_x - N_y)M_y)},$$

where  $N_x$ ,  $N_y$ , and  $N_z$  are the demagnetization factors along  $x$ -,  $y$ - and  $z$ -directions, respectively, and these factors obey the relation  $N_x + N_y + N_z = 4\pi$ . The total effective field is denoted by  $H_{eff}$  which includes applied bias field ( $H_{app}$ ) and stray field ( $H_S$ ), i.e.,  $H_{eff} = H_{app} \pm H_{S,y}$ . Here,  $H_{app} = 0$  as we are only interested in the remanent states so that there is no bias magnetic field present during the operation. Therefore, the direction of the stray field and its amplitude will mainly govern the change in the resonant frequencies from one remanent state to other. For a simplistic comparison, we have compared the experimental results with a rectangular nanomagnet of a similar dimension for which one can calculate the demagnetization factors using the formulations derived by Aharoni.<sup>69</sup> We obtain  $\Delta f = 210 \text{ MHz}$  for a field of 50 Oe, which is close to the value for the stray field estimated in Fig. 1(g). In the PQ network, it should result in twice the frequency shift ( $2 \times \Delta f = 420 \text{ MHz}$ ) because of the magnetic orientations of each

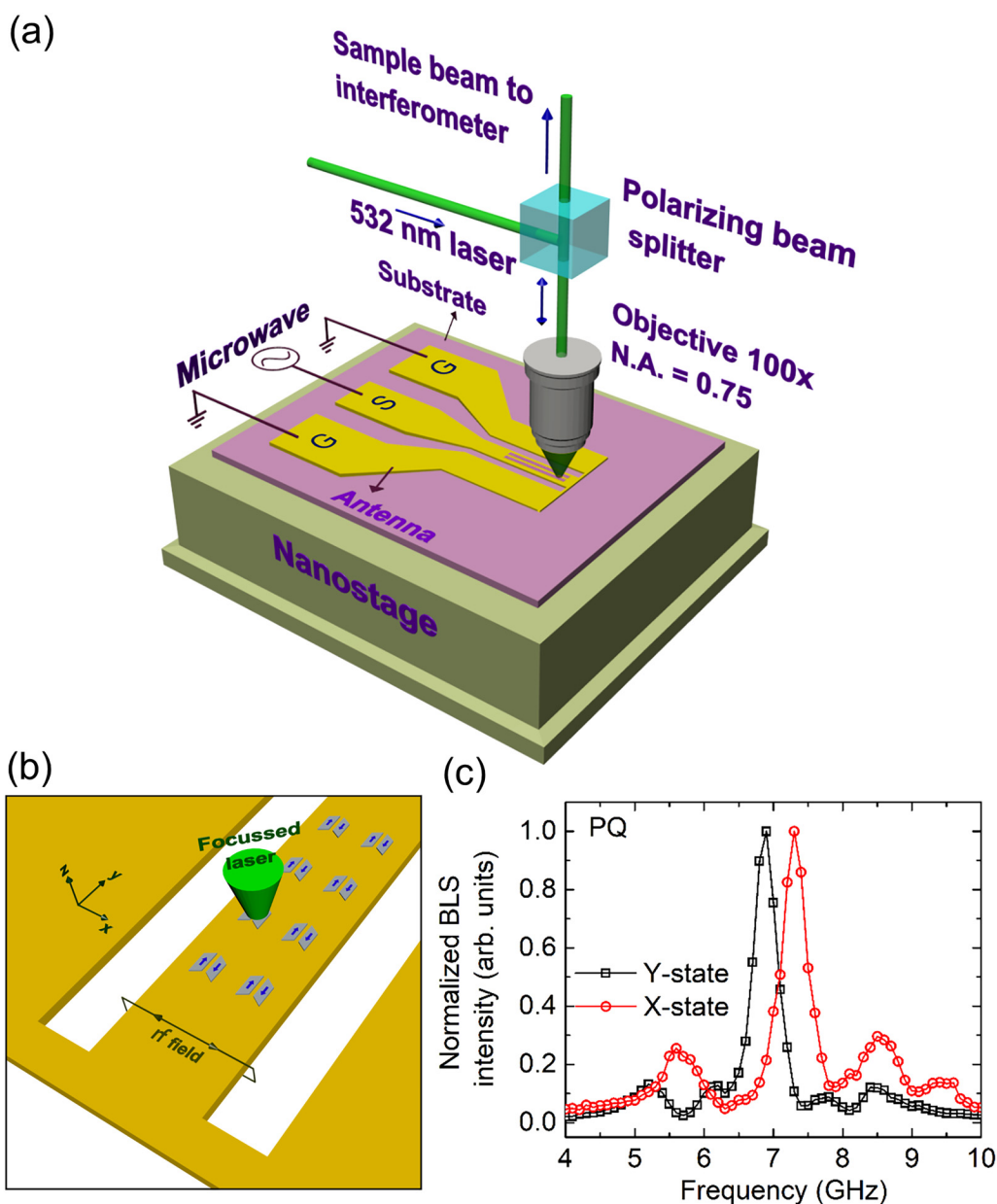


**FIG. 3.** (a) Schematic of the micro-BLS experiment for the detection of FMR modes. (b) A zoomed in view of the shorted CPW on which the PQ networks are patterned along with the micro-BLS laser spot. (c) Micro-BLS spectra obtained from a single nanomagnet pair for two different remanent states. Reproduced with permission from Haldar and Adeyeye, *ACS Nano* **10**, 1690–1698 (2016). Copyright 2016 ACS Publishing LLC.

other. Note that, analytical calculations based on stray field variations account for the observed BLS spectra shift of 400 MHz. Thus, just by using a pair of two RNMs (PQ), one can obtain tunable microwave properties by simply switching between two different remanent states, and it is also promising for reconfigurable microwave devices at nanoscale.

#### IV. TWO-DIMENSIONAL AFM-TYPE CRYSTALS BASED ON RNMs

We have found that the RNMs stabilize into a unique magnetic remanent state for the initialization along their short axes irrespective of their dipolar coupled neighbors in the network. However, the dipolar interaction was found to play a key role in

realizing distinct FMR responses with a predictable frequency shift. Therefore, RNMs offer a natural possibility of creating complex remanent magnetic states which are elusive via dipolar coupling based architectures. Based on these results, we have designed different types of antiferromagnetic-type states as the X-states as shown in Fig. 4(a) using blue arrows.<sup>61</sup> According to this X-state configuration, we have fabricated five different metamaterials (S1–S5) and the SEM images are shown in Fig. 4(a). RNMs have the same dimensions as mentioned above. The inter-element separations along the  $x$  axis ( $\delta_x$ ) and  $y$  axis ( $\delta_y$ ) are 110 nm and 75 nm for all

the samples except for S3, where  $\delta_y$  is 120 nm. Note that  $\delta_y$  indicates the shortest distance between the nanoelements. Two different remanent states (X-state and Y-state) are obtained by using the same procedure as mentioned above. MFM images for the X-state show AFM-type remanent states [Fig. 4(b)] with magnetic configurations as designed in Fig. 4(a). On the other hand, MFM images of the Y-state [Fig. 4(c)] show that all magnetizations are in the same directions. We would like to emphasize here that such complex AFM-type orientations have been observed without any error or unpredictable magnetic orientations over a large area. This

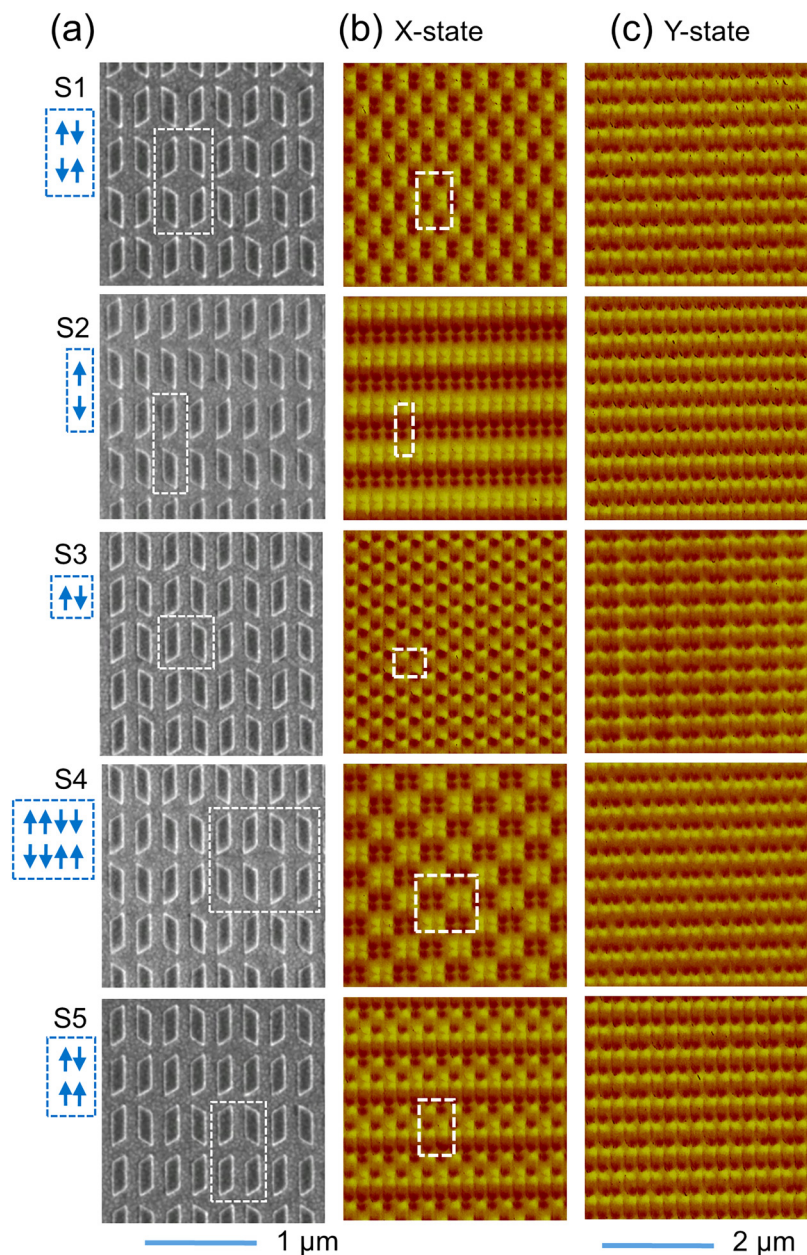


**FIG. 4.** (a) SEM images of five different types of 2D antiferromagnetic-type crystals based on RNMs. MFM images at two different remanent states: (b) X-state and (c) Y-state obtained for  $x$  axis and  $y$  axis initializations, respectively. Reproduced with permission from Haldar and Adeyeye, *Appl. Phys. Lett.* **108**, 022405 (2016). Copyright 2016 AIP Publishing LLC.

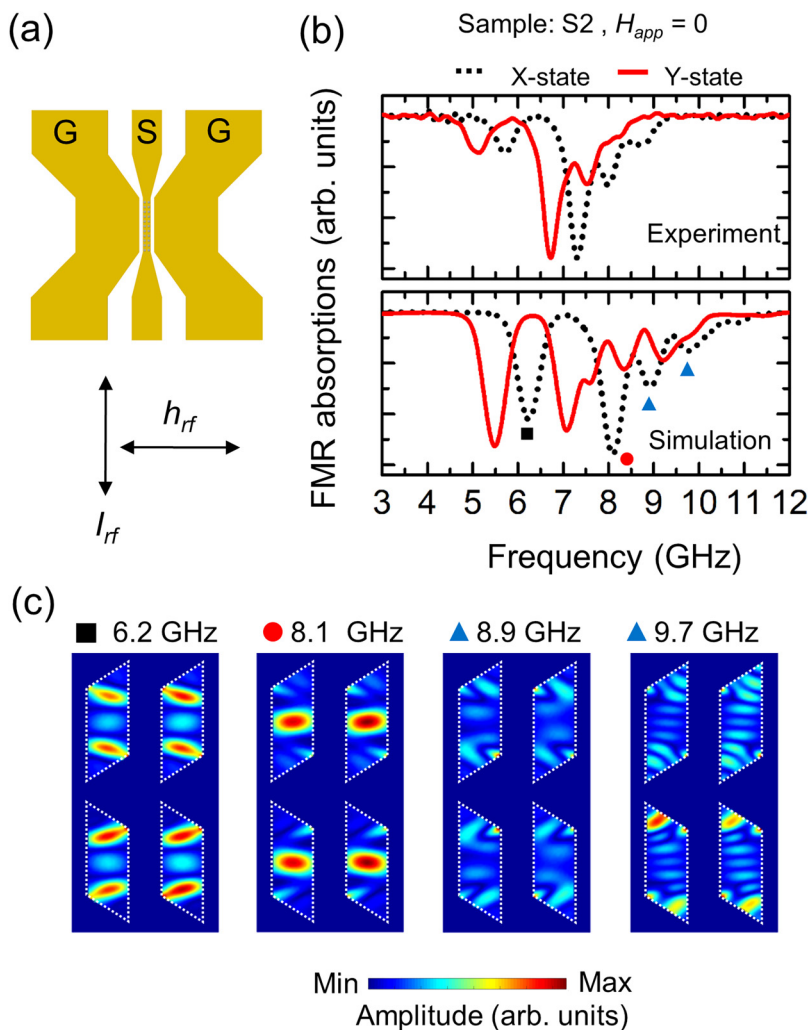


**FIG. 5.** (a) Schematic of a GSG-type CPW for FMR measurements. (b) Experimental and simulated FMR spectra at X-state and Y-state for the AFM crystal S2. (c) Simulated spatial profiles of different types of the resonant modes as marked by different symbols in the spectra. Reproduced with permission from Halder and Adeyeye, *Appl. Phys. Lett.* **108**, 022405 (2016). Copyright 2016 AIP Publishing LLC.

is remarkable as dipolar coupling driven remanent states are susceptible to fabrication defects. Therefore, the benefits of the shape anisotropy driven tunable remanent states are evident, and they are suitable for practical implementation in nanomagnetic devices.

The resonant modes of the isolated RNMs have also been measured using a vector network analyzer based ferromagnetic resonance (VNA-FMR) experiment by fabricating the nanomagnets on top of a coplanar waveguide (CPW) whose ports are connected to the VNA [Fig. 5(a)]. Note that the applied field was swept along both  $x$  axis and  $y$  axis directions during the VNA-FMR measurements from  $-1400$  Oe  $\rightarrow 0 \rightarrow 1400$  Oe. Experimental FMR spectra for both the remanent states (X-state and Y-state) are shown in Fig. 5(b) for the AFM crystal “S2.” Similar to the networks of RNMs, one can clearly see FMR shift while going from X-state to the Y-state. In order to identify the modes without any ambiguity, simulated FMR spectra were analyzed and the 2D spatial maps of the prominent modes are plotted in Fig. 5(c). The modes marked by “■” and “●” are found to be concentrated near the edges and center of the RNMs, respectively.

The ▲-labeled modes have nodal across the samples. The frequency shift between the two remanent states is  $\sim 600$  MHz. The experimental values are consistent with the simulated results with slight variation of the  $\Delta f$  values, which is expected to be due to unavoidable lithographic non-uniformities and averaging of the FMR signal from a large area sample. Nevertheless, demonstration of such complex AFM states using RNMs opens up possibilities for designing customized magnetic configurations for different applications.

## V. FERRIMAGNETIC-TYPE CRYSTALS BASED ON RNMs

We have seen that RNMs are robust for designing complex magnetic remanent states without any defect over a large area. Here, we discuss yet another interesting magnetic configuration which has a ferrimagnetic-type orientation—a well-known magnetic state with uncompensated anti-parallel magnetizations. In order to achieve it based on the RNMs, we have used two different widths of the RNMs and arranged them periodically as a 2D



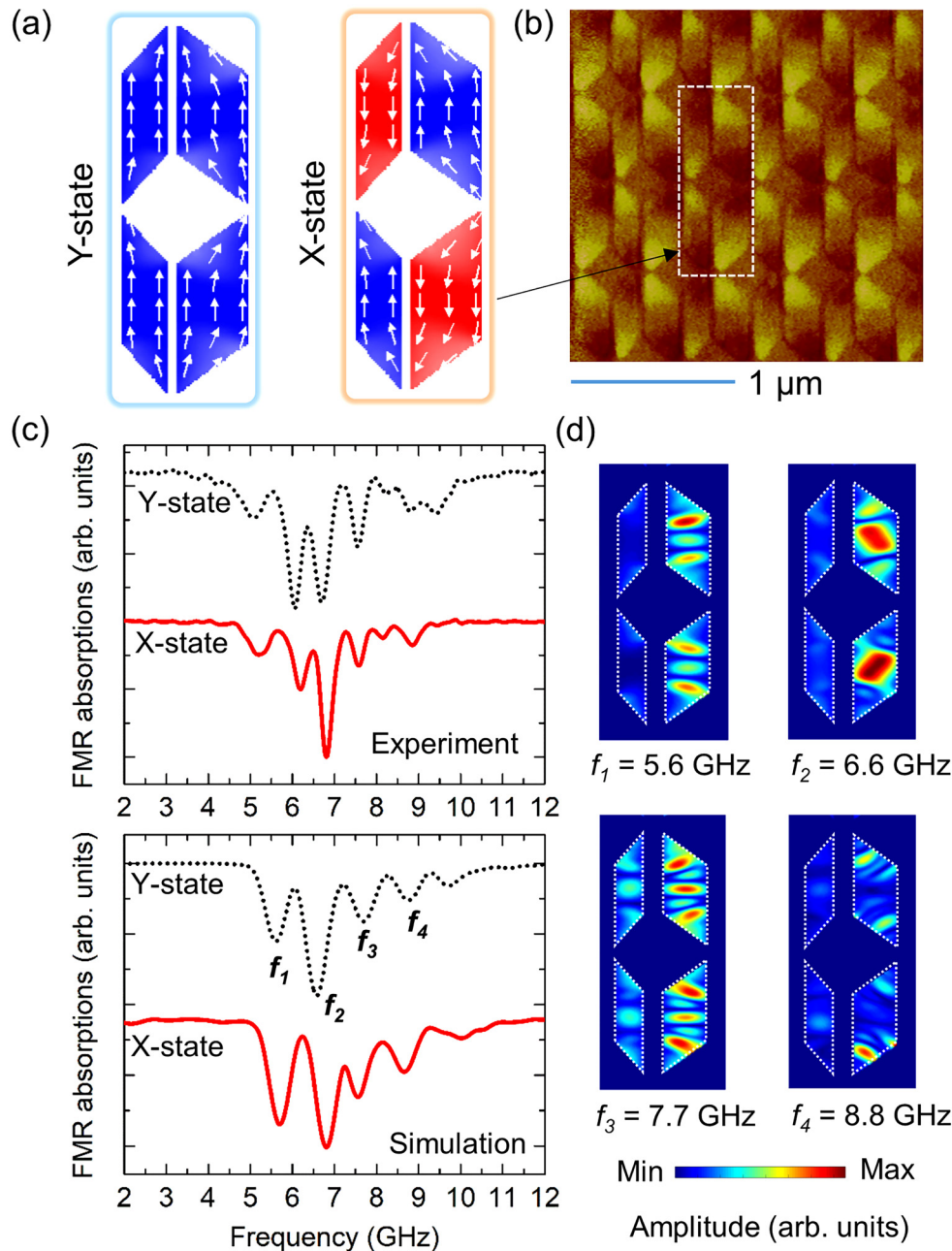


**FIG. 6.** (a) Simulated remanent states showing ferrimagnetic type ordering for the X-state. (b) MFM image of the ferrimagnetic-type remanent state. (c) Experimental and simulated FMR spectra at two different remanent states. (d) Simulated spatial profiles of different types of the resonant modes as marked for the Y-state. Reproduced with permission from Haldar and Adeyeye, *J. Appl. Phys.* **123**, 243901 (2018). Copyright 2018 AIP Publishing LLC.

crystal as shown in Fig. 6(a).<sup>52</sup> The dimensions of the RNMs are  $(u \times w \times \theta) = (320 \text{ nm} \times 170 \text{ nm} \times 35^\circ)$  and  $(320 \text{ nm} \times 110 \text{ nm} \times 48^\circ)$  for wide and thin RNMs, respectively. The thickness of the RNMs is 25 nm. The inter-element separations along the  $x$ - and

$y$ -directions are  $\delta_x = 80 \text{ nm}$  and  $\delta_y = 70 \text{ nm}$ , respectively. The same initialization process has been used in order to obtain the X-state and the Y-state. An MFM image for the X-state is shown in Fig. 6(b). We have found two-step reversals for the long axis ( $H_{app} \parallel y$ -axis)

hysteresis loops due to two different switching fields for two different widths of the RNMs in the array. Experimental FMR spectra for both the remanent states are shown in Fig. 6(c), and the results are compared with simulated FMR spectra. There are four prominent modes ( $f_1$ – $f_4$ ) which are identified by analyzing 2D spatial maps as shown in Fig. 6(d). It can be seen that mode  $f_1$  is located near the edges of the RNMs. Modes  $f_2$  and  $f_3$  are concentrated at the center of the wide and thin RNMs, respectively. Mode  $f_4$  has nodal lines in the wide RNMs, and it is located near the center of the thin RNMs. It should be noted here that the mode profiles have mixed signatures of edge- and center-type mode features in contrast to the AFM-type arrays discussed in the previous section. The frequency shift ( $\Delta f$ ) between the X-state and the Y-state is found to be 100 MHz (for the mode at  $f_2$ ), which is slightly lower than the shift obtained from simulations. The origin of the frequency shift can be attributed to the variation of the stray field which enhances or reduces the effective magnetic field ( $H_{eff}$ ). The  $\Delta f$  value can be optimized by increasing the stray field interactions by reducing the separation between the nanoelements. We have found a significant increase (three-times larger) of  $\Delta f = 600$  MHz for the inter-element separation  $\delta$  ( $= \delta_x = \delta_y$ ) = 30 nm. Note that the design of the array [Fig. 6(a)] only allows ferrimagnetic-type coupling along the  $x$  axis; however, the coupling is AFM-type along the  $y$  axis. A 2D ferrimagnetic-type crystal can be realized by interchanging the thin RNM with wide RNM and vice versa in one of the rows in the unit cell.

## VI. MULTILAYER RNMs AND THEIR DIPOLAR COUPLED NETWORKS

Note that a large frequency shift ( $\Delta f$ ) is desirable for unambiguous reconfigurable operations based on FMR responses. The parameter,  $\Delta f$  can be increased by reducing the inter-element separation for the above-mentioned samples. However, a smaller gap between the elements is susceptible to lithographic fabrication defects. Therefore, multilayer RNMs are explored where a smaller physical separation can be achieved by inserting a thin non-magnetic (NM) spacer layer. Moreover, it is less prone to lithographic variations over a large area. Below, we detail our demonstration based on multilayer RNMs and the observation of remarkably large FMR shifts.

Figure 7(a) shows different types of RNM multilayer combinations and their networks.<sup>65</sup> Isolated multilayer nanomagnets consisting of trilayer, five layers, and nine layers are denoted by 3L-1M, 5L-1M, and 9L-1M, respectively (first number represents the number of magnetic layers and second number represents the number of multilayer nanomagnets). Networks of two magnets (3L-2M), three magnets (3L-3M), four magnets (3L-4M), and two magnets with width modulations (3L-2M<sup>+</sup>) are also designed for tunable microwave properties. Two different remanent states have been obtained by initializing the RNMs along their short axis (X-state) and long axis (Y-state) as mentioned above. Magnetic configurations for the X-state are included in Fig. 7(a) for different layers. Note that AFM-type orientation has been found in all three spatial directions for the 3L-4M sample. Simulated FMR spectra are shown in Fig. 7(b) in the 3–15 GHz frequency range for both the Y-state (dotted line) and the X-state (solid line) in the absence of any external bias magnetic field ( $H_{ext} = 0$ ). We have seen a clear shift between the spectra for

X-state and Y-state. The modes are identified by plotting their spatial profiles followed by marking them with different symbols. The modes marked by “▲” and “●” symbols are concentrated near the edges and central parts of the RNMs, respectively. The most prominent modes are labeled by “■” symbols which are found to have nodal lines across the RNMs. The frequency shifts ( $\Delta f$ ) for the ■-mode are found to be 1.9, 3.5, 1.7, and 2.7 GHz for 3L-1M, 3L-2M, 3L-3M, and 3L-4M samples, respectively. A small  $\Delta f_{\blacksquare}$  of 0.3 GHz is found for the 3L-2M<sup>+</sup> sample. On the other hand, the mode profiles of 5L-1M and 9L-1M samples are found to have mixed signatures of different types of modes. However, a giant  $\Delta f$  of 4.9 GHz has been recorded for the most prominent mode for the 5L-1M sample. Observed frequency shifts are explained in terms of the variation of the effective field due to the stray field variations due to the dipolar coupled multilayer and network structures in Ref. 65.

Experimental demonstration of the RNM multilayers has been carried out by fabricating samples on top of a shorted CPW as shown in Fig. 3(a).<sup>63</sup> The multilayer RNM consists of Py (25 nm)/Cr ( $t_{Cr}$ )/Py (20 nm). The thickness of Cr is in the range from 0 to 15 nm. The lateral dimensions of the RNM were set to  $300 \times 130$  nm<sup>2</sup> ( $u \times w$ ). Two different remanent states have been stabilized by initializing the RNMs along their short (X-state) and long (Y-state) axes. Two magnetic layers align parallel (FM) and anti-parallel (AFM) to each other for the long axis and short axis initializations, respectively for  $t_{Cr} = 15$  nm. However, we have found anti-parallel orientation for both the initializations in the case of  $t_{Cr} = 5$  nm. This is due to a strong coupling between the magnetic layers for a small separation which stabilizes to an energetically favorable anti-parallel (AFM) remanent state. Micro-BLS spectra for two different initializations (long axis and short axis) are shown in Fig. 8(a) from a single isolated RNM multilayer for  $t_{Cr} = 0, 5$ , and 15 nm. A single prominent resonance peak at 9.8 GHz is observed for  $t_{Cr} = 0$ . No shift in the spectra is expected here for the two initializations as it represents a single layer RNM. The peak positions are at 7.7, 11.1, and 12 GHz for  $t_{Cr} = 5$  nm and no shift is expected here as well due to the AFM remanent state obtained irrespective of the initialization field orientation. We have found that the peaks at 9.1 GHz for the long axis have shifted to 11 GHz for the short axis in the case of  $t_{Cr} = 15$  nm. Thus, a remarkably large frequency shift ( $\Delta f$ ) of 1.9 GHz for  $t_{Cr} = 15$  nm is experimentally measured from a single isolated multilayer RNM. We have further investigated 3L-2M sample experimentally as a function of initialization field as shown in Fig. 8(b).<sup>64</sup> The magnetization orientations in each nanomagnet are denoted following the notation of  $\begin{pmatrix} P_{top} & Q_{top} \\ P_{bottom} & Q_{bottom} \end{pmatrix}$ . The FM remanent state  $\begin{pmatrix} \downarrow & \downarrow \\ \downarrow & \downarrow \end{pmatrix}$  was obtained using  $H_{ini} (-2000 \text{ Oe} \rightarrow 0)$  applied along the long axis of the nanomagnets. The AFM1 ground state was obtained using  $H_{ini} (-2000 \text{ Oe} \rightarrow 0)$  applied along the short axis. The AFM1 state can be expressed in  $\begin{pmatrix} \downarrow & \uparrow \\ \downarrow & \uparrow \end{pmatrix}$ . Note that the AFM ordering is in the in-plane direction and there is a FM ordering along the out-of-plane direction for the AFM1 state. We can obtain an AFM2 state by applying  $H_{ini} (-2000 \text{ Oe} \rightarrow 0 \rightarrow +350 \text{ Oe} \rightarrow 0)$  along the long axis. AFM2 state can be expressed

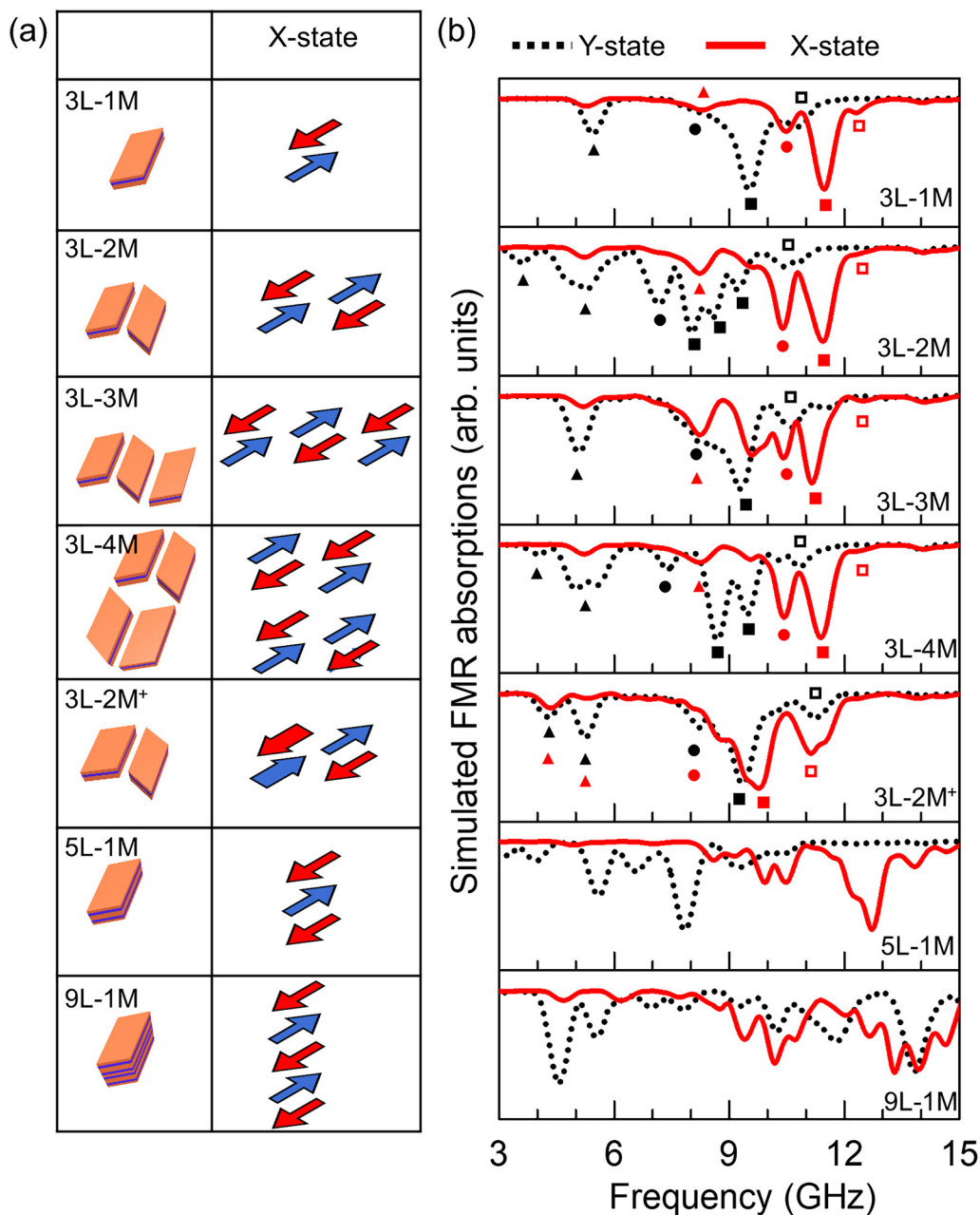


**FIG. 7.** (a) Schematics of different types of multilayer RNM configurations and anti-parallel magnetic orientations at the X-state. (b) Simulated FMR spectra for isolated and different types of multilayer RNM networks. Reproduced with permission from Begari and Haldar, *J. Phys. D Appl. Phys.* **51**, 275004 (2018). Copyright 2018 IOP Publishing LLC.

in  $\left( \begin{array}{c} \uparrow \\ \downarrow \\ \uparrow \\ \downarrow \end{array} \right)$ . Note that the AFM ordering is in the out-of-plane direction, and there is a FM ordering in the in-plane direction for the AFM2 state. Micro-BLS spectra from a single 3L-2M sample are shown in Fig. 8(c) for FM, AFM1, and AFM2 states. A single

prominent resonance peak at 8.2 GHz is observed for the FM state. This peak position is shifted to 9.6 GHz for the AFM1 state. The resonance peak is further shifted to 11 GHz for the AFM2 state. Thus, the amount of  $\Delta f$  is 2.8 GHz between the FM and AFM2 configurations. The large frequency shift for the AFM2

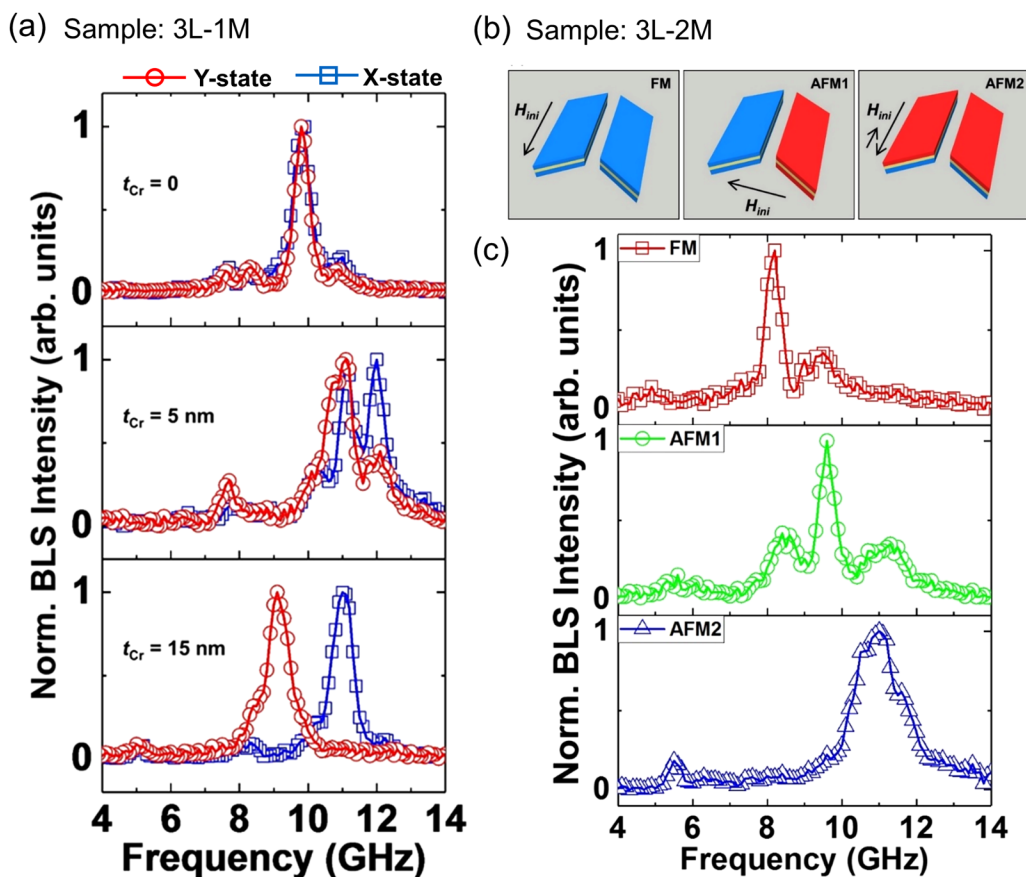


**FIG. 8.** (a) Micro-BLS spectra from a single multilayer RNM by varying the spacer layer. (b) Multilayer PQ-RNM pair as a function of initialization field. (c) Micro-BLS spectra of the resonant modes for multilayer PQ-RNM pair as a function of initialization field. Reproduced with permission from Chang and Adeyeye, *Appl. Phys. Lett.* **111**, 152404 (2017) and Chang and Adeyeye, *Appl. Phys. Lett.* **111**, 262402 (2017). Copyright 2017 AIP Publishing LLC.

state can be attributed to the anti-parallel orientation between the two magnetic layers as compared to the AFM1 state, where a parallel orientation is found. Thus, multilayer RNMs and their networks open up the possibilities of customized magnetic orientations in all three spatial directions and a 3D AFM-type crystal is proposed in Ref. 65.

## VII. USE OF SELF-BIASED RECONFIGURABLE RNMs IN A MAGNONIC DEVICE

Self-biased magnets also have applications in biasing operations in dipolar coupler nanomagnetic logic networks.<sup>70</sup> We have shown, in Ref. 71, the use of RNMs in controlling the vortex circularity by placing P- and Q-type RNMs on either sides of the magnetic disk. Recently, we proposed, in Ref. 66 that dipolar coupled chains of RNMs are suitable as a waveguide for magnon transport without bias magnetic field. We also use the reconfigurable remanent state to demonstrate gating operations in a magnonic device.

### A. Bias free waveguide for spin waves

Anisotropic spin-wave dispersion requires orthogonal configurations for spin-wave wave-vector and magnetization direction for efficient spin-wave propagation in nanomagnetic devices. This configuration is well-known as surface spin-wave mode. As a consequence, a prohibitively large bias magnetic field (typically 500–1200 Oe) is used, so far, for any demonstration of spin-wave transport.<sup>6,72–76</sup> This is a major obstacle for the practical implementation of magnetic devices particularly at nanoscale. An alternative to the bias field is shown by using an Oersted field generated by an underlying current line.<sup>77</sup> However, this bias current may have adverse effects due to Joule heating. Therefore, a waveguide without any bias field or current is of great interest. We have used the self-biased RNMs to design waveguide for spin waves by creating a chain of dipolar coupled but physically separated RNMs as shown in Fig. 9.<sup>66</sup> A shorted CPW is used for the excitation of spin waves in the nanowire. For the direct measurement of spin wave propagation, we have employed micro-BLS technique.

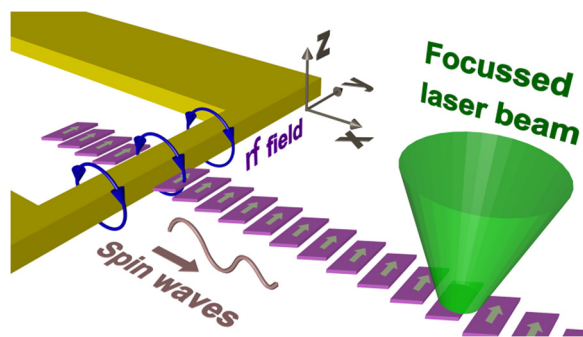


**FIG. 9.** Schematic of the micro-BLS experiment for the detection of propagating spin waves in a nanowire based on coupled RNMs. A shorted CPW is used to excite spin waves in the nanowire. Reproduced with permission from Haldar *et al.*, *Nat. Nanotech.* **11**, 437 (2016). Copyright 2016 Nature Publishing LLC.

SEM image of the waveguide along with an excitation antenna is shown in Fig. 10(a). The length ( $L$ ), width ( $W$ ), thickness ( $t$ ), and angle ( $\Phi$ ) of the slanted edge of a single RNM are 600 nm, 260 nm, 25 nm, and  $32^\circ$ , respectively. The separation ( $\delta$ ) between the nanomagnets was set to 50 nm in order to ensure strong dipolar coupling between the RNMs. The width ( $d$ ) of the antenna is  $1\ \mu\text{m}$  which can excite spin wave up to  $2\pi/d = 6.2\ \text{rad}/\mu\text{m}$ . Figure 10(b) shows the Y-state magnetization where all the RNMs have the same magnetic orientations. Note that the same initialization scheme was used as mentioned above. Shown in Fig. 10(c) is a micro-BLS spectrum which reveals significant spin wave propagation at 4.2 GHz. The propagation profiles of the spin wave at 4.2 GHz have been mapped on the right and the left sides of the antenna by scanning the laser beam [Fig. 10(d)]. One can notice spatial decay of the spin wave intensity. It can be fitted to an exponential decay function  $\exp(-2x/\xi)$ , where  $\xi$  is the decay length which represents the distance, where the intensity drops by

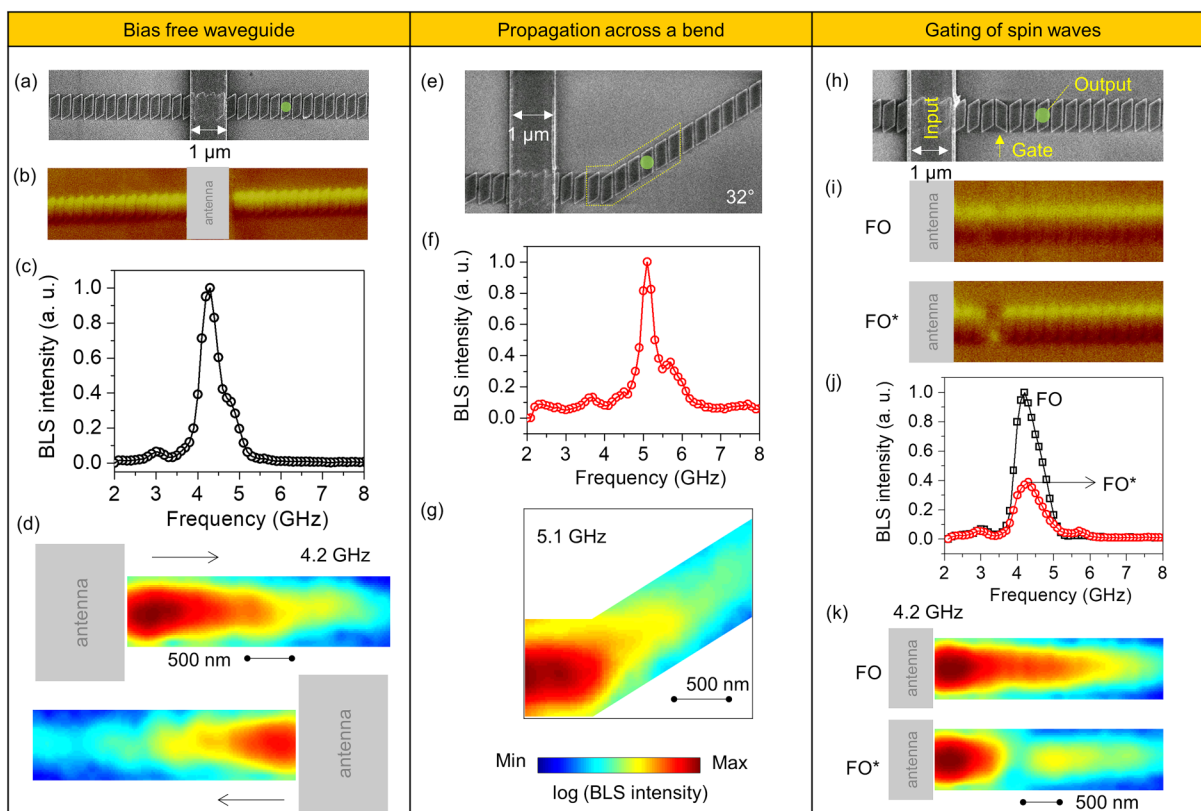


**FIG. 10.** (a) SEM image of the nanowire made from dipolar coupled RNMs. An excitation antenna is placed in the middle of the wire for the generation of spin waves. (b) MFM image at remanence showing all the magnets pointing in the same directions. (c) BLS spectra at remanence recorded at the green spot on the SEM image. (d) Experimental 2D spatial profiles of the spin wave intensity (4.2 GHz) on both sides of the antenna. (e) SEM image of a nanowire with a bend. (f) BLS spectra at remanence of this bend nanowire at the green spot. (g) Experimental 2D spatial map of the spin wave intensity (5.1 GHz) at the region as marked in the SEM image. (h) SEM image of a nanowire with a gate by designing a mirrored RNM. (i) MFM image showing ferromagnetically ordered (FO) state achieved by an initialization field applied along the long axis of the RNMs. (j) MFM image showing a flipped magnetization at the gate position (FO\*) achieved by an initialization field applied along the short axis. (k) BLS spectra for FO and FO\* states. (l) Experimental 2D spatial maps of the spin wave intensity at 4.2 GHz showing gated spin propagation for the FO\* state. Reproduced with permission from Haldar *et al.*, *Nat. Nanotech.* **11**, 437 (2016). Copyright 2016 Nature Publishing LLC.

a factor of  $e$ . The results clearly demonstrate spin wave transmission without any bias field.

### B. Spin wave propagation across a bend

It is necessary to send a signal at an angle for any devices. Likewise, magnonic devices also demand transferring signal in an arbitrary direction which is not trivial as magnon dispersion is highly anisotropic. Thereby, it was achieved by using a current line underneath the magnetic waveguide to produce a local Oersted field to align the spin perpendicular to the propagation direction.<sup>78</sup> It is important to explore the channeling spin waves at an angle without any stand-by power.

We utilize the same waveguide concept as discussed above to design a waveguide with an angle ( $32^\circ$ ) as seen from the SEM image in Fig. 10(e). Spin wave transmission is found to occur at 5.1 GHz as recorded by the micro-BLS spectrum [Fig. 10(f)]. 2D spatial profiles of the spin wave propagation are shown in Fig. 10(g) illustrating spin transmission across a bend without applying any bias field/current. This is another major development which also shows the versatility of our waveguide design concept.

### C. Gating of spin waves

For any digital functionalities, local manipulation of information in an energy-efficient manner is highly desirable. Demonstration of spin wave logic gates in the macro-scale devices have been shown in the past.<sup>13,14</sup> Recently, all magnonic transistor operation has been reported by creating a magnonic crystal in a mm-scale waveguide and using non-linear spin wave properties of the spin waves.<sup>12</sup> Note that in addition to a stand-by bias field, another power is required to be continuously turned on for the gating operation in these devices. A device which once initialized, manipulates signal without consuming energy will be ideal for computationally demanding applications.

We experimentally demonstrated binary gating of output signal amplitudes by switching one of the nanomagnets in the waveguide by selectively orienting the nanomagnets as shown in Fig. 10(h) marked as “gate.” Note that no stand-by power is needed once the waveguide is initialized. Two different field initializations—same as mentioned above—have been used to obtain Y-state and X-state. All the RNMs point in the same direction for the Y-state and it is denoted by ferromagnetically ordered (FO) state [Fig. 10(i)]. On the other hand, X-state has all the RNM point in the same direction except one RNM (marked as “gate”) which points in the opposite direction due to its opposite orientation with respect to the initialization field. The X-state magnetization is denoted by a FO state with a defect as FO\* [Fig. 10(i)]. This concept can be easily implemented for on-chip clocking using cross-point current lines or spin transfer torque switching.<sup>79</sup> Micro-BLS spectra in Fig. 10(j) show spin wave transmission at 4.2 GHz for the same waveguide but for the two remanent states, FO and FO\*. One can clearly see a significant drop in the spin wave intensity for the FO\* state as compared to the FO state. In order to understand this, one should look at the 2D spatial maps [Fig. 10(k)] of the 4.2 GHz mode recorded by micro-BLS imaging technique. One can see a discontinuous spin wave map for the FO\* state and the spin wave intensity vanishes at the gate position where magnetization has been flipped. However, spin waves propagate with a reduced intensity beyond the gate position (away

from the antenna) and it has been attributed to the wave phenomena such as reflection and tunneling. Recently, we have shown the spin wave gating in the same waveguide by switching the nanomagnets using high power microwave current.<sup>67</sup>

## VII. CONCLUSION

Miniaturization of the microwave devices and their integration on-chip alongside active components present a variety of challenges which provide further opportunities to explore new design architectures and search for new materials. Self-biased nanomagnetic networks and arrays with multiple remanent states associated with distinct dynamics are promising for downscaling the size of the device. However, the loss parameters in a microwave device needs to be optimized. Magnetic ferrites have been the choice for a microwave component due to their excellent insertion loss and isolation characteristics. Recent development on the ultra-thin film growth of low damping magnetic ferrites and their patterned structures may lead to the successful implementation of the microwave components on-chip.<sup>76,80–83</sup> The above results also demonstrate that a reconfigurable operation can be achieved by using a single nanomagnet (single layer or multi-layer) which open up the possibility of shrinking a microwave component in sub-micron scale. Demonstration of antiferromagnetic type magnetic orientation in all three spatial directions in a multi-layer nanomagnetic network opens up the 3D magnonic architecture. The ease of reconfigurability with a single step initializing field is discussed which is suitable for practical implementation with reliable operations. The proposed nanomagnetic structures provide a guideline for systemizing the search for more robust designs for shape induced magnetic remanent states with distinct dynamic properties suitable for reconfigurable microwave operation. Based on these working principles, we have also shown C-, L-, and S-type nanomagnetic networks for such tunable operations.<sup>84</sup> Beyond dipolar coupling based dynamics using interacting nanomagnets, we also demonstrated reconfigurable operations based on a single nanomagnet design such as arrow shaped<sup>85</sup> structures and zigzag nanowires.<sup>86</sup> Here, we stabilize different non-uniform magnetic remanent states deterministically and the FMR shift is an outcome of the variation of the demagnetization fields rather than dipolar fields in previous demonstrations.

We believe that the above-mentioned results will lead to demonstrations of new alternative methodologies to achieve reconfigurable microwave properties without a bias field. In this regard, we would like to point here that there are a lot of developments in exotic spin textures and their experimental realizations. For instance, skyrmion gyrotropic resonances occur at few GHz frequencies and the skyrmion modes strongly depend on the anisotropy, magnetic field, and dc current.<sup>87–89</sup> Therefore, microwave responses of the skyrmions can be reconfigured by using a variety of external means such as dc electric current, voltage controlled anisotropy, or bias field. Another alternative could be domain wall based dynamics in a nanowire where the different location of the domain wall which can be controlled by using a pulse current, can produce different microwave responses.<sup>90</sup> Other than these spin textures, voltage controlled magnetic anisotropy and strain induced magnetic reconfiguration can potentially be employed for reconfigurable microwave operations.<sup>91–96</sup> The search for bias-free

nanomagnetic structures for reconfigurable microwave properties also offers their suitability in magnonic devices for spin wave transport and gating applications. A dipolar coupled linear chain of rhomboid nanomagnets is one such example shown here. Thus, the results discussed above provide additional opportunities to exploit self-biased nanomagnetic structures with exotic spin textures for both microwave magnetics and nano-magnonic devices.

## ACKNOWLEDGMENTS

A.H. would like to acknowledge funding under the Early Career Research Award (No. ECR/2017/000571) and Ramanujan Fellowship (No. SB/S2/RJN-118/2016), Department of Science and Technology (DST). A.O.A. would like to acknowledge funding from the Royal Society and Wolfson Foundation.

## DATA AVAILABILITY

The data that support the findings of this study are available from the corresponding author upon reasonable request.

## REFERENCES

- <sup>1</sup>B. Dieny, I. L. Prejbeanu, K. Garello, P. Gambardella, P. Freitas, R. Lehnndorff, W. Raberg, U. Ebels, S. O. Demokritov, J. Akerman, A. Deac, P. Pirro, C. Adelmann, A. Anane, A. V. Chumak, A. Hirohata, S. Mangin, S. O. Valenzuela, M. C. Onbaşlı, M. d'Aquino, G. Prenat, G. Finocchio, L. Lopez-Diaz, R. Chantrell, O. Chubykalo-Fesenko, and P. Bortolotti, *Nat. Electron.* **3**, 446 (2020).
- <sup>2</sup>D. Sander, S. O. Valenzuela, D. Makarov, C. H. Marrows, E. E. Fullerton, P. Fischer, J. McCord, P. Vavassori, S. Mangin, P. Pirro, B. Hillebrands, A. D. Kent, T. Jungwirth, O. Gutfleisch, C. G. Kim, and A. Berger, *J. Phys. D: Appl. Phys.* **50**, 363001 (2017).
- <sup>3</sup>E. Y. Vedmedenko, R. K. Kawakami, D. D. Sheka, P. Gambardella, A. Kirilyuk, A. Hirohata, C. Binek, O. Chubykalo-Fesenko, S. Sanvito, B. J. Kirby, J. Grollier, K. Everschor-Sitte, T. Kampfrath, C.-Y. You, and A. Berger, *J. Phys. D: Appl. Phys.* **53**, 453001 (2020).
- <sup>4</sup>A. Hirohata, K. Yamada, Y. Nakatani, L. Prejbeanu, B. Diény, P. Pirro, and B. Hillebrands, *J. Magn. Magn. Mater.* **509**, 166711 (2020).
- <sup>5</sup>S. Bhanja, D. K. Karunaratne, R. Panchumarthy, S. Rajaram, and S. Sarkar, *Nat. Nanotechnol.* **11**, 177 (2016).
- <sup>6</sup>A. V. Chumak, V. I. Vasyuchka, A. A. Serga, and B. Hillebrands, *Nat. Phys.* **11**, 453 (2015).
- <sup>7</sup>V. V. Kruglyak, S. O. Demokritov, and D. Grundler, *J. Phys. D: Appl. Phys.* **43**, 264001 (2010).
- <sup>8</sup>A. Barman and A. Haldar, "Time domain study of magnetization dynamics in magnetic thin films, micro- and nanostructures," *Solid State Physics*, R. Stamps and R. Camley editors (Elsevier, 2014), Vol. 65, pp. 1–108.
- <sup>9</sup>B. Lenk, H. Ulrichs, F. Garbs, and M. Münzenberg, *Phys. Rep.* **507**, 107 (2011).
- <sup>10</sup>D. Grundler, *Nat. Phys.* **11**, 438 (2015).
- <sup>11</sup>C. Liu, J. Chen, T. Liu, F. Heimbach, H. Yu, Y. Xiao, J. Hu, M. Liu, H. Chang, T. Stueckler, S. Tu, Y. Zhang, Y. Zhang, P. Gao, Z. Liao, D. Yu, K. Xia, N. Lei, W. Zhao, and M. Wu, *Nat. Commun.* **9**, 738 (2018).
- <sup>12</sup>A. V. Chumak, A. A. Serga, and B. Hillebrands, *Nat. Commun.* **5**, 4700 (2014).
- <sup>13</sup>A. Khitun, M. Bao, and K. L. Wang, *J. Phys. D: Appl. Phys.* **43**, 264005 (2010).
- <sup>14</sup>T. Schneider, A. A. Serga, B. Leven, B. Hillebrands, R. L. Stamps, and M. P. Kostylev, *Appl. Phys. Lett.* **92**, 022505 (2008).
- <sup>15</sup>S. Klingler, P. Pirro, T. Brächer, B. Leven, B. Hillebrands, and A. V. Chumak, *Appl. Phys. Lett.* **106**, 212406 (2015).
- <sup>16</sup>T. Fischer, M. Kewenig, D. A. Bozhko, A. A. Serga, I. I. Syvorotka, F. Ciubotaru, C. Adelmann, B. Hillebrands, and A. V. Chumak, *Appl. Phys. Lett.* **110**, 152401 (2017).
- <sup>17</sup>V. G. Harris, *IEEE Trans. Magn.* **48**, 1075 (2012).
- <sup>18</sup>A. V. Chumak, A. A. Serga, and B. Hillebrands, *J. Phys. D: Appl. Phys.* **50**, 244001 (2017).
- <sup>19</sup>Z. K. Wang, V. L. Zhang, H. S. Lim, S. C. Ng, M. H. Kuok, S. Jain, and A. O. Adeyeye, *ACS Nano* **4**, 643 (2010).
- <sup>20</sup>M. Krawczyk and D. Grundler, *J. Phys. Condens. Matter* **26**, 123202 (2014).
- <sup>21</sup>G. Shimon, A. Haldar, and A. O. Adeyeye, "Chapter 4: Magnetization dynamics of reconfigurable 2D magnonic crystals," in *Spin wave confinement: Propagating spin waves*, S. O. Demokritov, editor (Pan Stanford Publishing, 2017), 2nd ed.
- <sup>22</sup>A. V. Chumak, A. A. Serga, and B. Hillebrands, *J. Phys. D: Appl. Phys.* **50**, 244001 (2017).
- <sup>23</sup>G. Gubbiotti, S. Tacchi, M. Madami, G. Carlotti, S. Jain, A. O. Adeyeye, and M. P. Kostylev, *Appl. Phys. Lett.* **100**, 162407 (2012).
- <sup>24</sup>S. Mamica, M. Krawczyk, M. L. Sokolovskyy, and J. Romero-Vivas, *Phys. Rev. B Condens. Matter Mater. Phys.* **86**, 144402 (2012).
- <sup>25</sup>A. O. Adeyeye and S. Jain, *J. Appl. Phys.* **109**, 07B903 (2011).
- <sup>26</sup>R. Zivieri, S. Tacchi, F. Montoncello, L. Giovannini, F. Nizzoli, M. Madami, G. Gubbiotti, G. Carlotti, S. Neusser, G. Duerr, and D. Grundler, *Phys. Rev. B Condens. Matter Mater. Phys.* **85**, 012403 (2012).
- <sup>27</sup>S. Neusser, G. Duerr, S. Tacchi, M. Madami, M. L. Sokolovskyy, G. Gubbiotti, M. Krawczyk, and D. Grundler, *Phys. Rev. B Condens. Matter Mater. Phys.* **84**, 184411 (2011).
- <sup>28</sup>J. W. Klos, D. Kumar, J. Romero-Vivas, H. Fangohr, M. Franchin, M. Krawczyk, and A. Barman, *Phys. Rev. B Condens. Matter Mater. Phys.* **86**, 184433 (2012).
- <sup>29</sup>H. Ulrichs, B. Lenk, and M. Münzenberg, *Appl. Phys. Lett.* **97**, 092506 (2010).
- <sup>30</sup>G. Duerr, M. Madami, S. Neusser, S. Tacchi, G. Gubbiotti, G. Carlotti, and D. Grundler, *Appl. Phys. Lett.* **99**, 202502 (2011).
- <sup>31</sup>K. L. Livesey, J. Ding, N. R. Anderson, R. E. Camley, A. O. Adeyeye, M. P. Kostylev, and S. Samarin, *Phys. Rev. B Condens. Matter Mater. Phys.* **87**, 064424 (2013).
- <sup>32</sup>Z. K. Wang, V. L. Zhang, H. S. Lim, S. C. Ng, M. H. Kuok, S. Jain, and A. O. Adeyeye, *ACS Nano* **4**, 643 (2010).
- <sup>33</sup>V. L. Zhang, H. S. Lim, C. S. Lin, Z. K. Wang, S. C. Ng, M. H. Kuok, S. Jain, A. O. Adeyeye, and M. G. Cottam, *Appl. Phys. Lett.* **99**, 143118 (2011).
- <sup>34</sup>M. Mruzckiewicz, M. Krawczyk, R. V. Mikhaylovskiy, and V. V. Kruglyak, *Phys. Rev. B Condens. Matter Mater. Phys.* **86**, 024425 (2012).
- <sup>35</sup>S. Tacchi, G. Duerr, J. W. Klos, M. Madami, S. Neusser, G. Gubbiotti, G. Carlotti, M. Krawczyk, and D. Grundler, *Phys. Rev. Lett.* **109**, 137202 (2012).
- <sup>36</sup>S. Saha, R. Mandal, S. Barman, D. Kumar, B. Rana, Y. Fukuma, S. Sugimoto, Y. Otani, and A. Barman, *Adv. Funct. Mater.* **23**, 2378 (2013).
- <sup>37</sup>J. W. Klos, M. L. Sokolovskyy, S. Mamica, and M. Krawczyk, *J. Appl. Phys.* **111**, 123910 (2012).
- <sup>38</sup>C. C. Wang, A. O. Adeyeye, and N. Singh, *Nanotechnology* **17**, 1629 (2006).
- <sup>39</sup>S. Tacchi, M. Madami, G. Gubbiotti, G. Carlotti, A. O. Adeyeye, S. Neusser, B. Botters, and D. Grundler, *IEEE Trans. Magn.* **46**, 1440 (2010).
- <sup>40</sup>J. Ding, M. Kostylev, and A. O. Adeyeye, *Phys. Rev. B Condens. Matter Mater. Phys.* **84**, 054425 (2011).
- <sup>41</sup>G. Gubbiotti, S. Tacchi, G. Carlotti, N. Singh, S. Goolaup, A. O. Adeyeye, and M. Kostylev, *Appl. Phys. Lett.* **90**, 092503 (2007).
- <sup>42</sup>Y. Filimonov, E. Pavlov, S. Vystostkii, and S. Nikitov, *Appl. Phys. Lett.* **101**, 242408 (2012).
- <sup>43</sup>V. G. Harris and A. S. Sokolov, *J. Supercond. Novel Magn.* **32**, 97 (2019).
- <sup>44</sup>M. Wu, in *Advances in Magnetic Materials*, edited by L. Malkinski (Intech, 2012).
- <sup>45</sup>See <https://www.mtmgx.com/> for "Metamagnetics Inc."
- <sup>46</sup>M. Darques, J. De La Torre Medina, L. Piroux, L. Cagnon, and I. Huynen, *Nanotechnology* **21**, 145208 (2010).
- <sup>47</sup>R. Verba, G. Melkov, V. Tiberkevich, and A. Slavin, *Appl. Phys. Lett.* **100**, 192412 (2012).

- <sup>48</sup>R. Verba, G. Melkov, V. Tiberkevich, and A. Slavin, *Phys. Rev. B* **85**, 014427 (2012).
- <sup>49</sup>G. Gubbiotti, P. Malagò, S. Fin, S. Tacchi, L. Giovannini, D. Bisero, M. Madami, G. Carlotti, J. Ding, A. O. Adeyeye, A. O. Adeyeye, and R. Zivieri, *Phys. Rev. B Condens. Matter Mater. Phys.* **90**, 024419 (2014).
- <sup>50</sup>G. Gubbiotti, H. T. Nguyen, R. Hiramatsu, S. Tacchi, M. G. Cottam, and T. Ono, *J. Magn. Magn. Mater.* **384**, 45 (2015).
- <sup>51</sup>J. Topp, D. Heitmann, M. P. Kostylev, and D. Grundler, *Phys. Rev. Lett.* **104**, 207205 (2010).
- <sup>52</sup>R. Huber, M. Krawczyk, T. Schwarze, H. Yu, G. Duerr, S. Albert, and D. Grundler, *Appl. Phys. Lett.* **102**, 012403 (2013).
- <sup>53</sup>J. Topp, S. Mendach, D. Heitmann, M. Kostylev, and D. Grundler, *Phys. Rev. B* **84**, 214413 (2011).
- <sup>54</sup>J. Ding, M. Kostylev, and A. O. Adeyeye, *Phys. Rev. Lett.* **107**, 047205 (2011).
- <sup>55</sup>J. Ding, M. Kostylev, and A. O. Adeyeye, *Appl. Phys. Lett.* **100**, 073114 (2012).
- <sup>56</sup>M. Vogel, A. V. Chumak, E. H. Waller, T. Langner, V. I. Vasyuchka, B. Hillebrands, and G. Von Freymann, *Nat. Phys.* **11**, 487 (2015).
- <sup>57</sup>O. Dzyapko, I. V. Borisenko, V. E. Demidov, W. Pernice, and S. O. Demokritov, *Appl. Phys. Lett.* **109**, 232407 (2016).
- <sup>58</sup>E. Albisetti, D. Petti, M. Pancaldi, M. Madami, S. Tacchi, J. Curtis, W. P. King, A. Papp, G. Csaba, W. Porod, E. Riedo, and R. Bertacco, *Nat. Nanotechnol.* **11**, 545 (2016).
- <sup>59</sup>A. V. Chumak, V. S. Tiberkevich, A. D. Karenowska, A. A. Serga, J. F. Gregg, A. N. Slavin, and B. Hillebrands, *Nat. Commun.* **1**, 141 (2010).
- <sup>60</sup>A. Haldar and A. O. Adeyeye, *ACS Nano* **10**, 1690 (2016).
- <sup>61</sup>A. Haldar and A. O. Adeyeye, *Appl. Phys. Lett.* **108**, 022405 (2016).
- <sup>62</sup>A. Haldar and A. O. Adeyeye, *J. Appl. Phys.* **123**, 243901 (2018).
- <sup>63</sup>C. Tian and A. O. Adeyeye, *Appl. Phys. Lett.* **111**, 152404 (2017).
- <sup>64</sup>C. Tian and A. O. Adeyeye, *Appl. Phys. Lett.* **111**, 262402 (2017).
- <sup>65</sup>K. Begari and A. Haldar, *J. Phys. D Appl. Phys.* **51**, 275004 (2018).
- <sup>66</sup>A. Haldar, D. Kumar, and A. O. Adeyeye, *Nat. Nanotechnol.* **11**, 437 (2016).
- <sup>67</sup>A. Haldar and A. O. Adeyeye, *Appl. Phys. Lett.* **116**, 162403 (2020).
- <sup>68</sup>C. Kittel, *Phys. Rev.* **73**, 155 (1948).
- <sup>69</sup>A. Aharoni, *J. Appl. Phys.* **83**, 3432 (1998).
- <sup>70</sup>M. T. Niemier, G. H. Bernstein, G. Csaba, A. Dangler, X. S. Hu, S. Kurtz, S. Liu, J. Nahas, W. Porod, M. Siddiq, M. Siddiq, and E. Varga, *J. Phys. Condens. Matter* **23**, 493202 (2011).
- <sup>71</sup>A. Haldar and A. O. Adeyeye, *Appl. Phys. Lett.* **106**, 032404 (2015).
- <sup>72</sup>S. Urazhdin, V. E. Demidov, H. Ulrichs, T. Kendziorczyk, T. Kuhn, J. Leuthold, G. Wilde, and S. O. Demokritov, *Nat. Nanotechnol.* **9**, 509 (2014).
- <sup>73</sup>T. Sebastian, Y. Ohdaira, T. Kubota, P. Pirro, T. Brächer, K. Vogt, A. A. Serga, H. Naganuma, M. Oogane, Y. Ando, and B. Hillebrands, *Appl. Phys. Lett.* **100**, 112402 (2012).
- <sup>74</sup>V. E. Demidov, S. O. Demokritov, K. Rott, P. Krzysteczko, and G. Reiss, *Phys. Rev. B Condens. Matter Mater. Phys.* **77**, 064406 (2008).
- <sup>75</sup>H. Yu, R. Huber, T. Schwarze, F. Brandl, T. Rapp, P. Berberich, G. Duerr, and D. Grundler, *Appl. Phys. Lett.* **100**, 262412 (2012).
- <sup>76</sup>P. Pirro, T. Brächer, A. V. Chumak, B. Lägel, C. Dubs, O. Surzhenko, P. Görnert, B. Leven, and B. Hillebrands, *Appl. Phys. Lett.* **104**, 012402 (2014).
- <sup>77</sup>K. Vogt, F. Y. Fradin, J. E. Pearson, T. Sebastian, S. D. Bader, B. Hillebrands, A. Hoffmann, and H. Schultheiss, *Nat. Commun.* **5**, 3727 (2014).
- <sup>78</sup>K. Vogt, H. Schultheiss, S. Jain, J. E. Pearson, A. Hoffmann, S. D. Bader, and B. Hillebrands, *Appl. Phys. Lett.* **101**, 042410 (2012).
- <sup>79</sup>D. Bhowmik, L. You, and S. Salahuddin, *Nat. Nanotechnol.* **9**, 59 (2014).
- <sup>80</sup>M. Evelt, C. Safranski, M. Aldosary, V. E. Demidov, I. Barsukov, A. P. Nosov, A. B. Rinkevich, K. Sobotkiewicz, X. Li, J. Shi, I. N. Krivorotov, and S. O. Demokritov, *Sci. Rep.* **8**, 1269 (2018).
- <sup>81</sup>B. Divinskiy, N. Thiery, L. Vila, O. Klein, N. Beaulieu, J. Ben Youssef, S. O. Demokritov, and V. E. Demidov, *Appl. Phys. Lett.* **116**, 062401 (2020).
- <sup>82</sup>M. Collet, X. De Milly, O. D'Allivy Kelly, V. V. Naletov, R. Bernard, P. Bortolotti, J. Ben Youssef, V. E. Demidov, S. O. Demokritov, J. L. Prieto, M. Muñoz, V. Cros, A. Anane, G. De Loubens, and O. Klein, *Nat. Commun.* **7**, 10377 (2016).
- <sup>83</sup>M. Collet, O. Gladii, M. Evelt, V. Bessonov, L. Soumah, P. Bortolotti, S. O. Demokritov, Y. Henry, V. Cros, M. Bailleul, V. E. Demidov, and A. Anane, *Appl. Phys. Lett.* **110**, 092408 (2017).
- <sup>84</sup>K. Begari and A. Haldar, *J. Phys. D Appl. Phys.* **52**, 335003 (2019).
- <sup>85</sup>A. Haldar and A. O. Adeyeye, *Appl. Phys. Lett.* **108**, 162401 (2016).
- <sup>86</sup>K. Begari and A. Haldar, *J. Phys. D Appl. Phys.* **53**, 455005 (2020).
- <sup>87</sup>C. H. Back, V. Cros, H. Ebert, K. Everschor-Sitte, A. Fert, M. Garst, T. Ma, S. Mankovsky, T. Monchesky, M. V. Mostovoy, N. Nagaosa, S. Parkin, C. Pfleiderer, N. Reyren, A. Rosch, Y. Taguchi, Y. Tokura, K. von Bergmann, and J. Zang, *J. Phys. D Appl. Phys.* **53**, 363001 (2020).
- <sup>88</sup>K. Everschor-Sitte, J. Masell, R. M. Reeve, and M. Kläui, *J. Appl. Phys.* **124**, 240901 (2018).
- <sup>89</sup>W. Jiang, P. Upadhyaya, W. Zhang, G. Yu, M. B. Jungfleisch, F. Y. Fradin, J. E. Pearson, Y. Tserkovnyak, K. L. Wang, O. Heinonen, S. G. E. te Velthuis, and A. Hoffmann, *Science* **349**(80), 283 (2015).
- <sup>90</sup>S. J. Hämäläinen, M. Madami, H. Qin, G. Gubbiotti, and S. van Dijken, *Nat. Commun.* **9**, 4853 (2018).
- <sup>91</sup>D. Bhattacharya, S. A. Razavi, H. Wu, B. Dai, K. L. Wang, and J. Atulasimha, *Nat. Electron.* **3**, 539 (2020).
- <sup>92</sup>S. Merabtine, F. Zighem, D. Faurie, A. Garcia-Sanchez, P. Lupo, and A. O. Adeyeye, *Nano Lett.* **18**, 3199 (2018).
- <sup>93</sup>N. D'Souza, M. Salehi Fashami, S. Bandyopadhyay, and J. Atulasimha, *Nano Lett.* **16**, 1069 (2016).
- <sup>94</sup>G. Dai, Q. Zhan, H. Yang, Y. Liu, X. Zhang, Z. Zuo, B. Chen, and R. W. Li, *J. Appl. Phys.* **114**, 173913 (2013).
- <sup>95</sup>C. Y. Liang, A. E. Sepulveda, D. Hoff, S. M. Keller, and G. P. Carman, *J. Appl. Phys.* **118**, 174101 (2015).
- <sup>96</sup>H. Ahmad, J. Atulasimha, and S. Bandyopadhyay, *Sci. Rep.* **5**, 18264 (2015).